

Optimizing compensation in Ising spin-1/2 site-diluted trilayered square ferrimagnets: Insights from Monte Carlo Simulations

Soham Chandra ^{*1}

¹*Department of Physics, Presidency University, 86/1 College Street, Kolkata -700 073, India*

Abstract

This study employs Monte Carlo simulations using the Metropolis algorithm to investigate the thermomagnetic properties of a site-diluted trilayered ferrimagnetic system with spin-1/2 particles placed on square monolayers. The system is composed of two different types of theoretical atoms, labeled A and B, resulting in two distinct configurations, ABA and AAB. Atoms of the same type (A-A and B-B) exhibit ferromagnetic interactions, while unlike atoms (A-B) display antiferromagnetic interactions. The A-layers are randomly site-diluted with non-magnetic atoms and the percentage of dilution is varied from 5% to 45%. Depending upon the concentration of these impurities, both the compensation and critical points shift, leading to different equilibrium ferrimagnetic behaviors. The phase area in the Hamiltonian parameter space, *without* compensation, scales according to the relation: $\ln |A(\rho)/\tilde{A}| = ae^{b\rho}$. Attention is paid to the mathematical relationships between the compensation temperature and the concentration of nonmagnetic impurities. Suggested mathematical formulas reveal how the threshold impurity concentration is linked to the Hamiltonian parameters.

Keywords: Spin-1/2 Ising square trilayer; quenched nonmagnetic impurities; Metropolis Monte Carlo simulation; Compensation temperature; Threshold concentration of impurities

arXiv:2503.18879v1 [cond-mat.stat-mech] 24 Mar 2025

*E-mail addresses: soham.rs@presiuniv.ac.in ; sohamc07@gmail.com

1 Introduction

The study of spin systems with antiferromagnetic coupling has gotten a lot of interest in condensed matter physics, especially since the discovery of ferrimagnetism in 1948 [1,2]. Ferrimagnetic systems display intriguing properties due to the interaction of existing ferromagnetic and antiferromagnetic intersite interactions. Furthermore, studying the magnetic characteristics of these systems aids in determining their prospective uses. A ferrimagnet is often modelled as a combination of two or more magnetic substructures, e.g., sublattices, sublayers or subsets of atoms. Among them, *layered* ferrimagnetic materials stand out due to their superior area-to-volume ratio. Thin ferrimagnets, a subclass of layered ferrimagnetic materials, with one dimension significantly smaller than the other two, act as a link between monolayer (2D) and bulk (3D) magnetic materials. In recent times a considerable theoretical attention is centered around the *compensation effect* in the layered thin ferrimagnets [3,4]. Different magnetic responses to the variation of temperature of component sublayers, when combined, lead to the appearance of compensation points, i.e., temperatures lower than the critical point for which magnetization of the total system is zero but the sublayers retain magnetic ordering. Such layered ferrimagnets with ferromagnetic and antiferromagnetic interactions have revealed interesting magnetic responses and phase diagrams. The layered ferrimagnets with interlayer antiferromagnetic coupling between adjacent ferromagnetic layers have been used in giant magnetoresistance (GMR) [11], magneto-optical recordings [12], the magnetocaloric effect [13] and spintronics [14]. As a result, recent experimental realizations include bilayer [15], trilayer [16,17], and multilayered [18–21] systems, with desired characteristics. Molecular-beam epitaxy (MBE) [22], metalorganic chemical vapour deposition (MOCVD) [23], pulsed laser deposition (PLD) [24], and Atomic layer deposition (ALD) [25,26] have been extensively used in growth of such thin films in recent times.

Besides experimental progress, theoretical investigations on such ferrimagnets are also equally important. But, despite the advancement of theoretical and computational techniques and their applications on different magnetic properties shown by these magnetic 2D and quasi-3D heterostructures, our theoretical understanding still has gaps to fill. For example, CrI_3 in bulk (3D) is ferromagnetic [27,28] but stacks of a few atomic layers show antiferromagnetic interlayer coupling [29]. Ferromagnetism in bulk and single-layer, CrI_3 , is reproduced by electronic structure calculations [30–34], but the same was unsuccessful in describing the antiferromagnetic interlayer exchange coupling of the bilayered version [35]. Structural anomaly in thin films could be one of the reasons behind this discrepancy [36,37]. Density functional theory combined with a Hubbard model (DFT + U), with the “around-mean-field” correction scheme, is able to describe the vertical magnetotransport which agrees with the experimental measurements of magnetoresistance in multilayered CrI_3 enclosed between graphene contacts [38]. A detailed investigation is carried out, in [39], with the (DFT + U) approach for the three *Cr* trihalides CrI_3 , CrBr_3 , and CrCl_3 to determine the type of magnetic exchange interactions and magnetic ordering temperatures. Let’s now see

how a few of the successful and popular theoretical techniques have treated different layered magnetic structures, using spin models. References [3,40–46] demonstrate the versatility of the *mean-field analysis* as a very successful semi-analytical method for establishing the thermodynamics of the magnetic systems. Furthermore, there are only a few analytical techniques that are exactly solvable for different spin-systems, such as the *generalized classical transfer matrix method and decoration-iteration mapping* [47–51], *Bethe ansatz-based quantum transfer matrix and nonlinear integral equations method* [52,53], the *Jordan-Wigner transformation* [54,55] etc. The technological aspects of such layered magnetic structures, e.g. the magnetocaloric effect in the spin-1 Blume-Capel model, is theoretically studied in [56], using the *mean-field theory from the Bogoliubov inequality*. In [57], the effect of *next nearest neighbour interactions* on compensation temperature and phase transition is investigated in a trilayered ferrimagnetic system on a square lattice, employing Metropolis Monte Carlo simulation. In [58], by Metropolis Monte Carlo simulation, in a *ABA*-type trilayered stacking with non-equivalent layers, dynamic magnetic response has been studied under a harmonically oscillating external magnetic field. Compensation phenomenon emerges in this system under the dynamic scenario along with dynamic phase transition (DPT). So, theoretical magnetic models are quite useful in providing physical insights into the compensation phenomenon and describing experimental data. Extensive search for novel, magnetically compensated materials exhibiting better performance is centered around the manipulation and control of compensation points [59,60], which is also the aim of this work.

Let us now look at some recent developments in diluted magnetic systems. The effect of site dilution on compensation and critical temperatures of a two-dimensional mixed spin-1/2 and spin-1 system has been studied using Monte Carlo simulations, in [61]. In [62], Monte Carlo simulation with Wolff cluster algorithm is employed to investigate the thermodynamic and magnetic properties of a *site diluted* spin-1/2 Ising multilayered ferrimagnet. The investigated system is made up of non-equivalent planes with quenched site diluted alternating planes having the dominant in-plane coupling. In [63], a Monte Carlo study of the magnetic properties of an Ising multilayer ferrimagnet is performed with two kinds of non-equivalent planes, one of which is site-diluted.

So previous results in the literature indicate that the magnetic properties of the thin magnetic systems with nonmagnetic impurities are interesting compared to their pristine counterparts. Such studies provide better insight into the physics behind real magnetic quasi-3D systems. In this work, we would use a Monte Carlo approach to investigate how the quenched non-magnetic disorder influences the compensation and critical properties of a diluted trilayered Ising spin-1/2 ferrimagnet on a square lattice. Our focus would be on:

- (a) How does the concentration of nonmagnetic impurities at the diluted planes affect the critical and compensation behaviour?
- (b) How would the phase diagram change with the change in the concentration of impurity?
- (c) Can we define any mathematical relationship between the physical properties of the system and the concentra-

tion of impurities?

By carefully selecting the appropriate interaction parameters and injecting random non-magnetic impurities, we can demonstrate that it is possible to design an Ising trilayered heterostructure on square Bravais lattice with desired compensation and critical temperatures and to analyse and describe the magnetic properties with complex interactions in a phenomenological perspective.

The rest of the paper is organized as follows: the magnetic model is explained in Section 2. The strategy of simulation for the trilayered system is presented in Section 3. The numerical results are presented and discussed in Section 4. The work is summarised in Section 5.

2 Theoretical Model

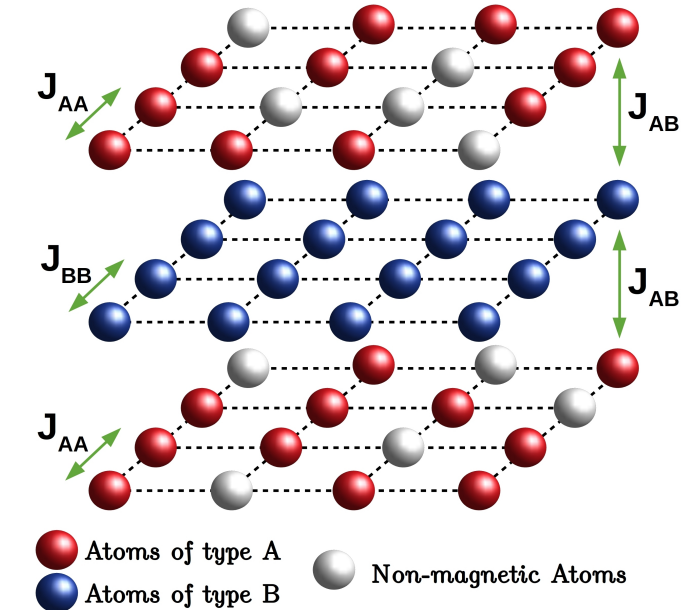
The focus of this article centers around a ferrimagnetic trilayer wherein magnetic atoms of spin-1/2 occupy specific locations within distinct square, parallel monolayers. In the ABA-type structure, consecutive planes are filled with either A or B theoretical atoms in an alternating pattern. In the AAB-type structure, the top and middle layers contain A-atoms while the lower layer contains B-type atoms. In both the setups, plane B remains unaffected with predominant in-plane coupling, while the A-planes experience site dilution due to the presence of nonmagnetic atoms at a concentration denoted by ρ . Figure [1] depicts a schematic representation of the trilayered arrangements.

Ising-like magnetic interactions are restricted to the nearest neighbours. There are two distinct types of magnetic interactions: (a) Between like atoms (A-A and B-B), it is Ferromagnetic; (b) Between different atoms (A-B), it is Anti-ferromagnetic. For such ferrimagnetic trilayered systems, with all of the S^z s being z components of spin moments on lattice sites, the Hamiltonian using nearest neighbour Ising mechanics [64] is as follows:

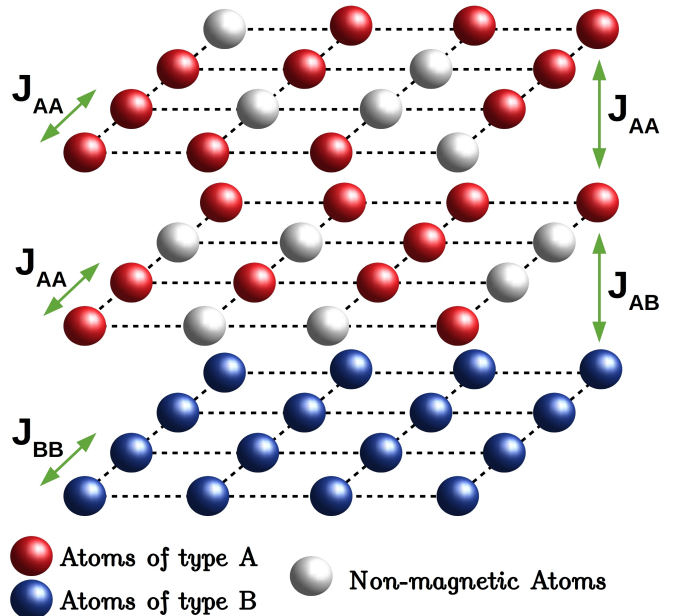
$$\begin{aligned}
 H_{ABA} = & -J_{AA} \left[\sum_{\langle t,t' \rangle} (\xi_t S_t^z)(\xi_{t'} S_{t'}^z) \right. \\
 & + \sum_{\langle b,b' \rangle} (\xi_b S_b^z)(\xi_{b'} S_{b'}^z) \left. \right] - J_{BB} \sum_{\langle m,m' \rangle} S_m^z S_{m'}^z \\
 & - J_{AB} \left[\sum_{\langle t,m \rangle} (\xi_t S_t^z) S_m^z + \sum_{\langle m,b \rangle} S_m^z (\xi_b S_b^z) \right] \quad (1)
 \end{aligned}$$

$$\begin{aligned}
 H_{AAB} = & -J_{AA} \left[\sum_{\langle t,t' \rangle} (\xi_t S_t^z)(\xi_{t'} S_{t'}^z) \right. \\
 & + \sum_{\langle m,m' \rangle} (\xi_m S_m^z)(\xi_{m'} S_{m'}^z) \left. \right] - J_{BB} \sum_{\langle b,b' \rangle} S_b^z S_{b'}^z \\
 & - J_{AA} \sum_{\langle t,m \rangle} (\xi_t S_t^z)(\xi_m S_m^z) \\
 & - J_{AB} \sum_{\langle m,b \rangle} (\xi_m S_m^z) S_b^z \quad (2)
 \end{aligned}$$

where J_{BB} (on the B-layer) and J_{AA} (on the A-layers) are the intra-layer ferromagnetic coupling strengths between the nearest neighbours. J_{AB} represents the inter-layer antiferromagnetic coupling strengths. Based on the nature of magnetic interactions, $J_{AA} > 0$, $J_{BB} > 0$, and $J_{AB} < 0$. $\langle t, t' \rangle$, $\langle m, m' \rangle$, and $\langle b, b' \rangle$ are the nearest



(a) ABA type of diluted trilayered stacking



(b) AAB type of diluted trilayered stacking

Figure 1: (Colour Online) Miniaturised versions ($3 \times 4 \times 4$) of *site-diluted*: (A) ABA-type and (B) AAB-type triangular trilayered Ising superlattices. Each of the sublattices of the ferrimagnetic systems are formed on triangular lattice. The actual simulation is carried out on a system with $N_{sites} = 3 \times 100 \times 100$.

neighbour summation indices for the top, mid, and bottom layers, respectively. Similarly, $\langle t, m \rangle$ and $\langle m, b \rangle$ imply summations over nearest-neighbor pairs in vertically adjacent layers. The governing parameters would be the ferromagnetic coupling ratio J_{AA}/J_{BB} and the antiferromagnetic coupling ratio J_{AB}/J_{BB} . We would also assume that J_{BB} is the dominant coupling strength of them all and set it to unity. The configurational averages of the occupancy probability of A-atoms for the ABA variant are $\bar{\xi}_t = \bar{\xi}_b = (1 - \rho)$, and for the AAB variant, they are

$\bar{\xi}_t = \bar{\xi}_m = (1 - \rho)$, with ρ : concentration of nonmagnetic atoms. The top and bottom layers don't interact with each other out of plane. In-plane, periodic boundary conditions and along the vertical, open boundary conditions will be used. Notations used here and subsequent sections are similar to the ones used in [10].

3 Simulation Protocol

Monte Carlo simulations with the Metropolis single-spin flip method [65, 66] are used to model the thermomagnetic behavior of the systems presented in Figure [1]. The total number of sites is $N_{sites} = 3 \times 100 \times 100$, with each plane having 100×100 sites on a square Bravais lattice structure. We conclude that the size of the lattice is statistically trustworthy for our purposes based on the considerations in Section ???. The z components of spin projections at the i -th site, S_{iz} with ($S_{iz} = \pm 1/2$), participate in Ising interactions. The system was initiated in a high-temperature paramagnetic phase by site-diluting a fraction ρ of randomly selected sites on the A-layers and from the remaining spin projections, half are in $S_{iz} = +1/2$ while the other half are in $S_{iz} = -1/2$. The B-layer is pristine and it has an equal population of $S_{iz} = +1/2$ and $S_{iz} = -1/2$. A trial configuration is now created by reorienting a randomly selected single spin. This trial configuration is accepted with probability, $p = \min\{1, e^{-\beta\Delta E}\}$, where ΔE denotes the energy difference between the trial and the present configuration. One Monte Carlo sweep (MCS) is composed of random single-spin updates that repeat $3L^2$ times. In this article, a single MCS serves as the unit of time.

At each temperature step, first 2×10^4 MCS are used for equilibration. From the next 8×10^4 MCS, we would acquire data after every 800 MCS for 100 *uncorrelated* configurations for essential physical quantities (to reduce the auto-correlation effect). The systems' last configuration at the previous higher temperature acts as the initial configuration for simulation at the next lower temperature. The dimensionless temperatures of the system are reported in units of J_{BB}/k_{BB} . The dominant exchange coupling of the B-layer, J_{BB} , serves as the unit of energy scale and is set to unity. The other coupling strengths, such as J_{AA} and J_{AB} , are measured relative to J_{BB} . The system is subject to periodic boundary conditions intra-plane (taken to be the x and y axes), while open boundary conditions are applied vertically (along the z axis). Seven distinct values of J_{AA}/J_{BB} and $|J_{AB}/J_{BB}|$ are considered, ranging from 0.04 to 1.0, with an interval of 0.16. We now define the time/ensemble averages of the observables to be measured during the numerical analysis.

(1) **Sublattice magnetizations** for the individual layers, after equilibration, are calculated at the i -th uncorrelated MCS, by:

$$m_{qi}(T) = \frac{1}{L^2} \sum_{x,y=1}^{L=100} (S_{qi}^z(T))_{xy} \quad (3)$$

The time (equivalently, ensemble) average (in angular braces) is obtained from the N uncorrelated configurations by:

$$\langle m_q(T) \rangle = \frac{1}{N} \sum_{i=1}^N m_{qi}(T) \quad (4)$$

In the above equations, q is the sublayer index. The order parameter of the trilayer, **time averaged total magnetisation**, $m_{tot}(T)$, at temperature, T , is defined as:

$$m_{tot}(T) = \frac{1}{3} (\langle m_t(T) \rangle + \langle m_m(T) \rangle + \langle m_b(T) \rangle) \quad (5)$$

(2) **Ensemble average of associative energy per site**, $\varepsilon(T)$, at temperature T is obtained after equilibration as:

$$\varepsilon(T) = \frac{\langle H(T) \rangle}{3L^2} \quad (6)$$

from the N uncorrelated MCS. Equations [1] and [2] are used here.

(3) **Magnetic susceptibility per site**, $\chi(T)$, after equilibration at temperature T , is obtained by:

$$\chi(T) = 3L^2 \frac{(\Delta m_{tot}(T))^2}{k_B T} \quad (7)$$

where, $\Delta m(T)$ is the fluctuation of the order parameter. Similarly, **Specific heat per site**, $C(T)$, after equilibration at temperature T , is obtained by:

$$C(T) = 3L^2 \frac{(\Delta \varepsilon(T))^2}{k_B T^2} \quad (8)$$

with, $\Delta \varepsilon(T)$ being the fluctuation of the associative energy per site. For any quantity, say, A , the relevant fluctuation at temperature T , $\Delta A(T)$, is determined by the following way:

$$\Delta A(T) = \sqrt{\frac{1}{N} \sum_{i=1}^N [A_i(T) - \langle A(T) \rangle]^2} \quad (9)$$

where $A_i(T)$ is the value of A after the i -th uncorrelated MCS.

(4) **The fourth order Binder cumulant**, $U_4(T)$, at dimensionless temperature T , after equilibration and for a given linear dimension, L , of the square lattice is defined as [66]:

$$[U_4(T)]_L = 1 - \frac{\langle m_{tot}^4(T) \rangle_L}{3 \langle m_{tot}^2(T) \rangle_L^2} \quad (10)$$

A single system size of $L = 100$ is used in this study. At each temperature step, averaging over 10 distinct sample realizations (identical macroscopic but different microscopic arrangements) are performed for each quantity. The associated errors are estimated using the Jackknife method [67] and are generally smaller than the point markers in the plots away from the critical point.

4 Results

4.1 Thermodynamic response

First, we discuss qualitatively the thermomagnetic response of both the configurations: ABA and AAB for three different dilution concentrations e.g. $\rho = \{0.00, 0.20, 0.40\}$.

A common feature we observe is the magnetization profiles [51] can be manipulated by changing either of the three controlling parameters: (i) the ferromagnetic ratio (FR), (J_{AA}/J_{BB}) (ii) the antiferromagnetic ratio (AFR), (J_{AB}/J_{BB}) and (iii) the concentration of non-magnetic impurities, ρ . In Figure [2], our focus is primarily on the dilution percentage, ρ . For an **ABA** configuration: in Figure [2](a), with FR= 0.52, we witness the number of magnetization profiles of N-type increases with increasing ρ and ultimately for $\rho = 0.40$, all the available magnetization profiles have compensation point associated with them, i.e. profiles of N-type and in Figure [2](b), with AFR= -0.36 , we witness magnetization profiles of N,R and Q-type in the pristine ($\rho = 0.0$) configuration and for $\rho = 0.20$ N and R-type of profiles are available and increasing ρ to 0.40, we have only N-type magnetization profiles. Similarly, for an **AAB** configuration, in Figure [2](c), (with, FR= 0.52) we witness N and R-type of magnetization profiles and the number of N-type magnetization profiles increases with increasing ρ and for $\rho = 0.20$ and $\rho = 0.40$, all the available magnetization profiles are of N-type and in Figure [2](d) (with, AFR= -0.36) we witness N, Q and P-type of magnetization profiles for the pristine stacking, for $\rho = 0.20$ we see N, R and Q profiles and for $\rho = 0.40$, all the available magnetization profiles are of N-type. In all of these instances, for pristine and diluted systems alike, the compensation points (when present) and critical temperatures shift to higher temperature values with increase in the magnitudes of ferromagnetic (J_{AA}/J_{BB}) and antiferromagnetic ($|J_{AB}/J_{BB}|$) ratios, when the concentration of non-magnetic impurities is kept fixed.

To study further, in Figure [3], we focus on how the magnetization profiles evolve as a function of concentration of non-magnetic impurities, when combinations of ferromagnetic and antiferromagnetic ratios are kept fixed. *For the ABA stacking:* in Figure [3](a) (with $J_{AA}/J_{BB} = 0.04$ and $J_{AB}/J_{BB} = -0.20$) we see only N-type magnetization profile with compensation temperature shifting to lower temperature values with increasing ρ . Plot of susceptibility versus temperature shows sharp peaks (signature of singularity) in the neighbourhood of the critical point and flattened peaks about the compensation point (see inset). In Figure [3](b) (with $J_{AA}/J_{BB} = 1.00$ and $J_{AB}/J_{BB} = -0.84$) we witness R-type magnetization profile (with no compensation point) transitioning into N-type (with single compensation temperature) with increasing ρ . For the R-type profiles, we see singularities in susceptibility and specific heat only about the transition temperature and for the N-type profile (with $\rho = 0.40$), additionally we see smeared peaks (see inset) about the compensation point. *For the AAB stacking:* in Figure [3](c) (with $J_{AA}/J_{BB} = 0.04$ and $J_{AB}/J_{BB} = -0.20$) we see N-type magnetization profiles with compensation points shifting towards lower temperature ends with increasing ρ . Sharp peaks in susceptibility and specific heat occur about the transition temperature and additionally we see smeared peaks (see inset) about the compensation point. In Figure [3](d) (with $J_{AA}/J_{BB} = 1.00$ and $J_{AB}/J_{BB} = -0.84$) we see Q-type magnetization profile (with $\rho = 0.00$ and no compensation point) transitioning into R-type (with $\rho = 0.20$ and no compensation point) and N-type (with $\rho = 0.40$ and single compensation

point). For all these profiles, susceptibility and specific heat show sharp peaks only about the transition temperature and only for the N-type profile, the curves flatten (see inset) about the compensation point.

At this point, we should closely concentrate on a few selected cases to understand distinct cases of how magnetization profiles continuously change with the concentration of non-magnetic impurities and what are the implications of that. For an ABA configuration: with weak coupling ratios ($J_{AA}/J_{BB} = 0.20$ and $J_{AB}/J_{BB} = -0.04$), in Figure [4](a) we see compensation points shifting towards lower temperature end for N-type magnetization profiles as we increase the concentration of non-magnetic impurities. In Figure [4](b), with strong coupling ratios ($J_{AA}/J_{BB} = 0.84$ and $J_{AB}/J_{BB} = -1.00$), we see Q and R-type profiles (with no compensation points) gradually transitioning into N-type magnetization profile (with single compensation point for $\rho = 0.35$ onwards) as we increase ρ . This is an example where we can create a compensation point by just adding quenched non-magnetic impurity. *Similar observation is true for the AAB configuration as well.* In Figure [4](c), with weak coupling ratios ($J_{AA}/J_{BB} = 0.20$ and $J_{AB}/J_{BB} = -0.04$), we see N-type magnetization profiles shift their compensation points towards lower temperature end with increase in the concentration of non-magnetic impurities. In Figure [4](d), strong coupling ratios ($J_{AA}/J_{BB} = 0.84$ and $J_{AB}/J_{BB} = -1.00$) coupled with increasing concentration of impurity, drive Q and R-type profiles (with no compensation points) into N-type magnetization profile (with single compensation point). So, we can also create a compensation point in AAB configuration by simply introducing quenched non-magnetic impurity.

We are now in a position to discuss how and when magnetization profiles change (from non-compensating to compensating) depending upon the concentration of quenched non-magnetic impurity, ρ . For example, we take Figure [5](a): with fixed $J_{AB}/J_{BB} = -0.52$ and for $\rho = 0.0$ (pristine sample), we don't see compensation points for $J_{AB} = -0.52$ and lower values. But, after introducing minimal nonmagnetic impurity ($\rho = 0.0$), compensation occurs at $J_{AA}/J_{BB} = 0.52$. As we continuously increase the concentration of impurity from here onto $\rho = 0.45$, we see stronger out-of-plane interactions gradually showing us compensation points e.g. from $\rho = 0.25$ and onwards, all the coupling combinations have compensation points attached to their magnetization profiles. All the other figures can be explained in similar manner. At this point, it is evident that the phase curve in the Hamiltonian parameter space is a function of concentration of non-magnetic impurities.

4.2 Phase diagrams

We have seen, in [6], how we draw the phase diagram in the Hamiltonian parameter space ($J_{AA} \times J_{AB}$). This work shows us introduction of non-magnetic impurities actually create compensation points in the thermomagnetic behaviour of the systems compared to their pure or pristine versions for distinct combinations of coupling ratios. Thus, in the Hamiltonian parameter space, the area where compensation is absent gradually shrinks as we increase the concentration of nonmagnetic impurities and beyond

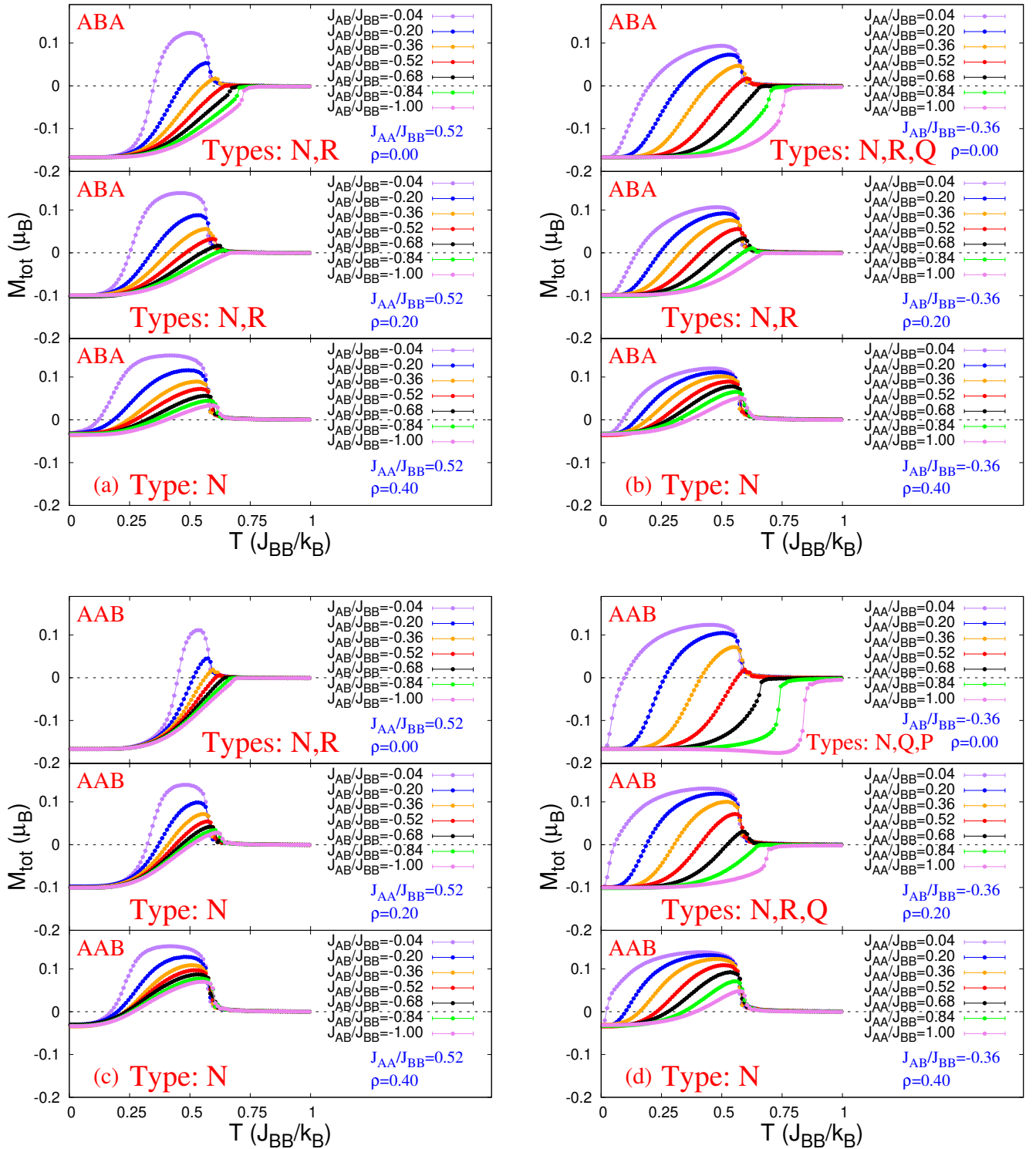


Figure 2: (Colour Online) Plots of total magnetisation, M_{tot} , versus reduced temperature, T , with three concentrations of non-magnetic impurities, ρ , for: (a) ABA: $J_{AA}/J_{BB} = 0.52$ and varying J_{AB}/J_{BB} ; (b) ABA: $J_{AB}/J_{BB} = -0.36$ and varying J_{AA}/J_{BB} ; (c) AAB: $J_{AA}/J_{BB} = 0.52$ and varying J_{AB}/J_{BB} ; (d) AAB: $J_{AB}/J_{BB} = -0.36$ and varying J_{AA}/J_{BB} .

a critical concentration of non-magnetic atoms, all distinct combinations of coupling strengths (within the range of this study) show compensation. For both ABA and AAB configurations, in Figures [6](a) and [6](c) respectively, the phase diagrams are plotted in the parameter space ($J_{AB}/J_{BB} \times J_{AA}/J_{BB}$). The phase curves divide the phase area into two parts: the A -marked areas, at the left

of the phase curves, denote the absence of compensation and the P -marked areas, at the right of the phase curves, show us the combinations of coupling strengths which has compensation associated with thermomagnetic response. To plot the fractional area of the non-compensating region, $A(\rho)/A_{tot}$, as a function of concentration of non-magnetic impurities, ρ , we find $A(\rho)$ by Monte Carlo inte-

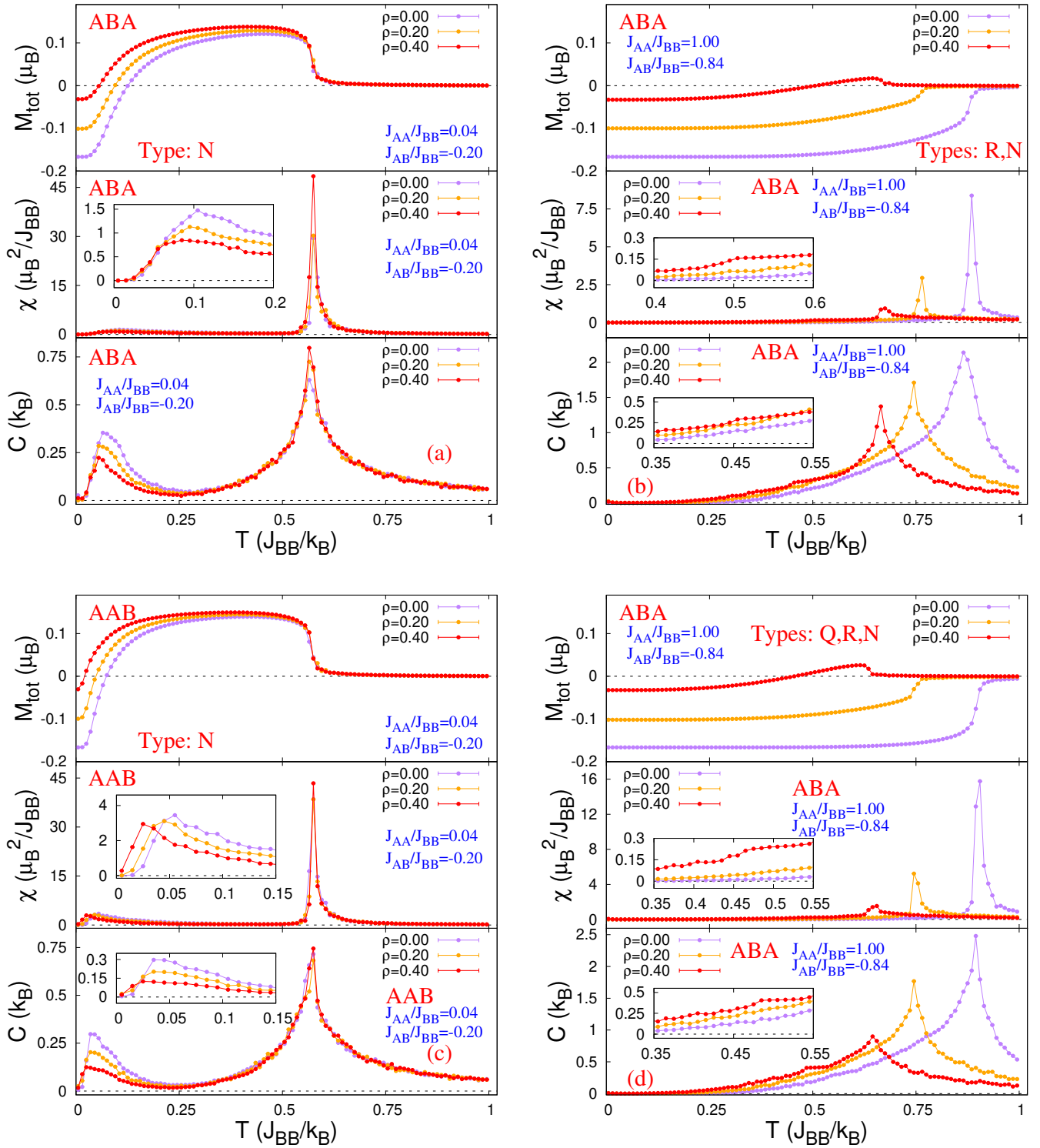


Figure 3: (Colour Online) Plots of total magnetisation, M_{tot} , magnetic susceptibility χ , and specific heat C versus reduced temperature, T , with three concentrations of non-magnetic impurities, ρ , for: (a) ABA: $J_{AA}/J_{BB} = 0.04$ and $J_{AB}/J_{BB} = -0.20$; (b) ABA: $J_{AA}/J_{BB} = 1.00$ and $J_{AB}/J_{BB} = -0.84$; (c) AAB: $J_{AA}/J_{BB} = 0.04$ and $J_{AB}/J_{BB} = -0.20$; (d) AAB: $J_{AA}/J_{BB} = 1.00$ and $J_{AB}/J_{BB} = -0.84$.

gration [68]. The impurity-driven changes in the relative areas in the Phase diagram are clearly visible in Figure [6](b) and (d). The technical details, in a similar situation, can be revisited in [10].

Now let us discuss about the fitting procedure and fitting parameters in detail. The generic form of such a quadratic fitting polynomial for both the configurations

is:

$$\left[\frac{J_{AA}}{J_{BB}}(\rho) \right]_{fit} = p(\rho) \left(\frac{J_{AB}}{J_{BB}} \right)^2 + q(\rho) \left(\frac{J_{AB}}{J_{BB}} \right) + r(\rho) \quad (11)$$

All the three fitting parameters are functions of concentration of non-magnetic impurities, ρ and their values and required statistical parameters are noted in Table [1].

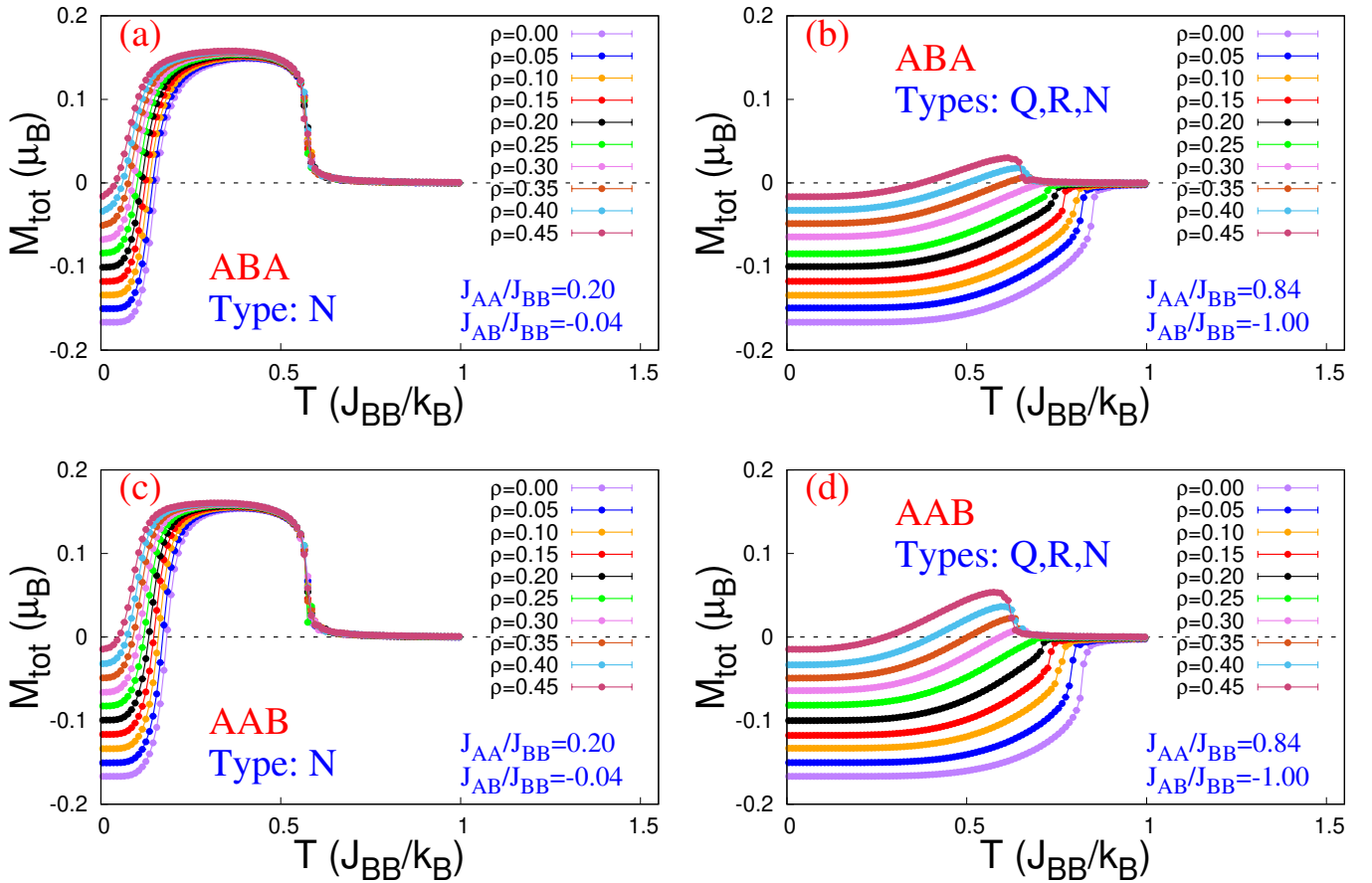


Figure 4: (Colour Online) Plots of total magnetisation, M_{tot} , versus reduced temperature, T , with concentration of non-magnetic impurities, ρ , as parameter for: (a) ABA: $J_{AA}/J_{BB} = 0.20$ and $J_{AB}/J_{BB} = -0.04$; (b) ABA: $J_{AA}/J_{BB} = 0.84$ and $J_{AB}/J_{BB} = -1.00$; (c) AAB: $J_{AA}/J_{BB} = 0.20$ and $J_{AB}/J_{BB} = -0.04$; (d) AAB: $J_{AA}/J_{BB} = 0.84$ and $J_{AB}/J_{BB} = -1.00$.

For ABA, a linear polynomial of the form: $f_1(\rho) = \left[\frac{A(\rho)}{A_{tot}} \right]_{ABA} = n_1\rho + l_1$; provides us with a critical concentration of, $\rho_{c,ABA} = 0.3186 \pm 0.0114$. For AAB, a quadratic polynomial of the form: $f_2(\rho) = \left[\frac{A(\rho)}{A_{tot}} \right]_{AAB} = m_2\rho^2 + n_2\rho + l_2$; provides us with a critical concentration of, $\rho_{c,AAB} = 0.3126 \pm 0.0462$. Above this *critical* concentration of non-magnetic atoms, every distinct combination of reduced coupling strengths show us magnetic compensation. So, we get an approximate maximum value of threshold concentration for both the configurations.

4.3 Systematics

In Figure [??], for a few representative cases, we see the variation of critical and compensation temperatures with the concentration of spin-0 atoms for a few distinct combinations of coupling strengths. For both ABA and AAB configurations, the compensation points *nonlinearly* vary with the increase in the concentration of spin-0 impurity, *till we reach the threshold concentration*. In this context, we can define the threshold concentration of non-magnetic impurity, for any combination of coupling strengths, to be the concentration of spin-0 atoms after attaining which we find *distinctly* different compensation and critical temperatures. For critical temperatures, the situation is a bit different. Till 45% dilution, for the weakest combi-

nation of coupling strengths, e.g. $J_{AA}/J_{BB} = 0.04$ and $J_{AB}/J_{BB} = -0.04$, the change in critical temperature is limited to within $\sim 1.74\%$ for both ABA and AAB configurations and for the strongest combination of coupling strengths, e.g. $J_{AA}/J_{BB} = 1.00$ and $J_{AB}/J_{BB} = -1.00$, the change in critical temperature is limited to within $\sim 27.32\%$ for ABA and within $\sim 29.51\%$ AAB configurations.

Now comes the question: How can we mathematically model the variation of compensation temperature with the concentration of non-magnetic impurities? In Figure [8], a quadratic polynomial is employed to mimic the behaviour and it can be seen that the approximation *statistically matches fairly well* with the simulation data.

For ABA:

$$T_{comp,ABA} \left(\rho, \frac{J_{AA}}{J_{BB}}, \frac{J_{AB}}{J_{BB}} \right) = p_1\rho^2 + q_1\rho + r_1 \quad (12)$$

For AAB:

$$T_{comp,AAB} \left(\rho, \frac{J_{AA}}{J_{BB}}, \frac{J_{AB}}{J_{BB}} \right) = p_2\rho^2 + q_2\rho + r_2 \quad (13)$$

The coefficients, namely, $p_i \equiv p_i(J_{AA}/J_{BB}, J_{AB}/J_{BB})$; $q_i \equiv q_i(J_{AA}/J_{BB}, J_{AB}/J_{BB})$; and $r_i \equiv r_i(J_{AA}/J_{BB}, J_{AB}/J_{BB})$ with $i \in \{1, 2\}$ explicitly depend upon the reduced coupling strengths, i.e. J_{AA}/J_{BB} , and J_{AB}/J_{BB} . A discussion on the fitting parameters [72] is provided in Appendix

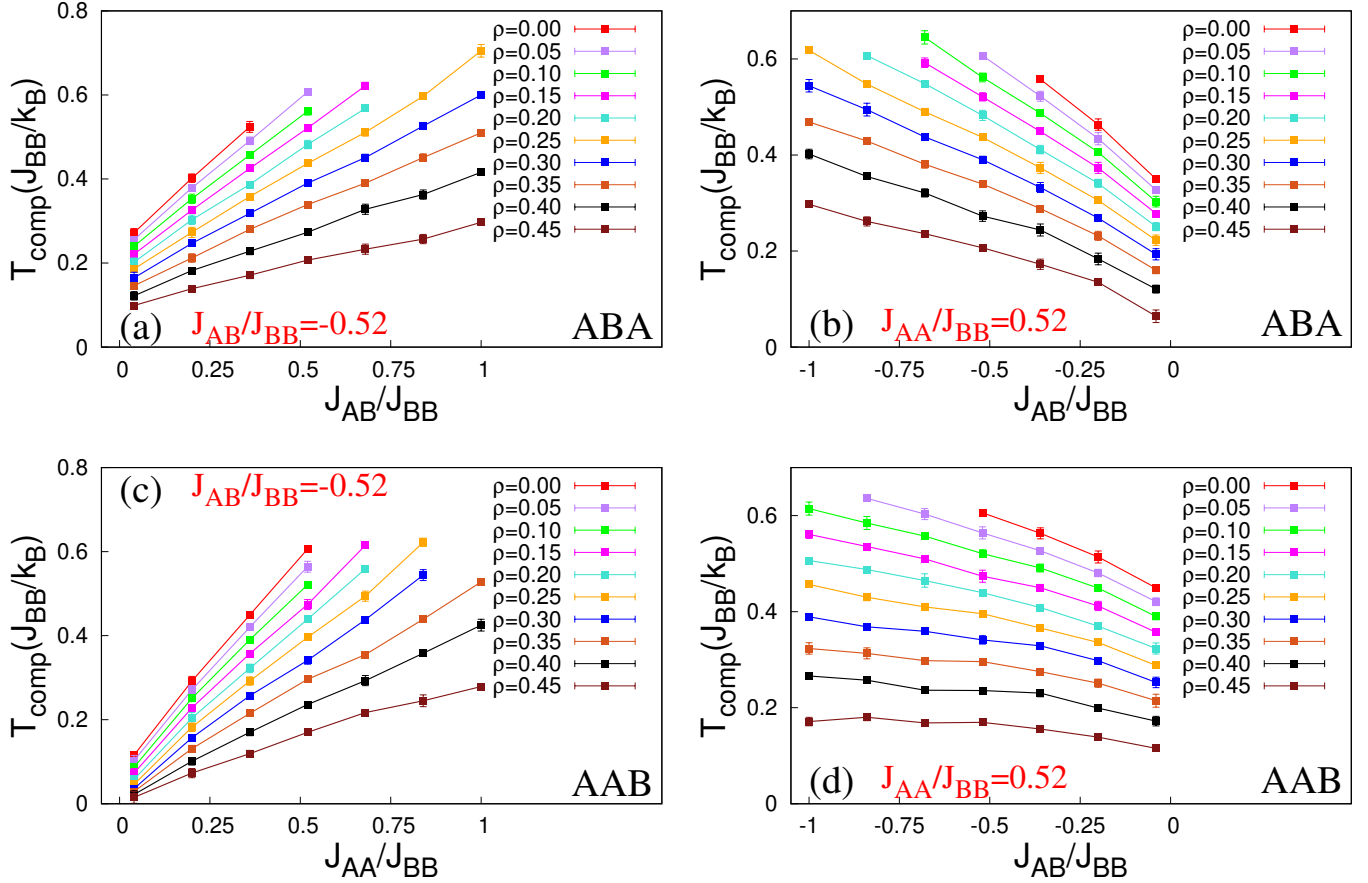


Figure 5: (Colour Online) Plots for, ABA stacking of (a) compensation temperature, T_{comp} , versus J_{AA}/J_{BB} , (b) compensation temperature, T_{comp} , versus J_{AB}/J_{BB} , and AAB stacking of (c) compensation temperature, T_{comp} , versus J_{AA}/J_{BB} , (d) compensation temperature, T_{comp} , versus J_{AB}/J_{BB} , with variable concentration of nonmagnetic impurities, ρ .

??, where we show the behaviours of the fitting parameters for both configurations.

At this point, we may try to find out any prevailing scaling relation between the magnitude of the phase area without compensation scale with the concentration of the non-magnetic impurities, ρ . This would be a 1D scaling, and the function can now be proposed as:

$$\ln \left| \frac{A(\rho)}{\tilde{A}} \right| = ae^{b\rho} \quad (14)$$

where a, b , and \tilde{A} are *scaling parameters* dependent on the type of configuration of the system, *ABA* and *AAB*. By regression analysis, we find the values of the scaling parameters and report them in Table [2]. In Figure [9], we can see the scaled values are well confined within the *fitted interval* which validates the hypothesis of Equation [14].

Now, we recall that threshold value of the concentration of nonmagnetic impurities is defined to be that particular value above which, for any distinct combination of the coupling strengths (equivalently, coupling ratios), we would have a compensation point associated with the thermomagnetic response. Evidently, threshold values of impurity concentrations explicitly depend on two Hamiltonian parameters, J_{AA}/J_{BB} and J_{AB}/J_{BB} . In Figure [10], we have a total of four plots (two each for *ABA* and *AAB* configurations) where we can try to estimate

the systematic variation of threshold concentration, ρ_T , with J_{AA}/J_{BB} and J_{AB}/J_{BB} . It is evident that as the magnitude of either of the coupling ratios increases, the value of ρ_T increases. Talking about the *ABA* configuration, now we can attempt to model the variation of ρ_T . Two functional variations may be proposed here, keeping in mind the Hamiltonian parameters, J_{AA}/J_{BB} and J_{AB}/J_{BB} , don't depend upon each other.

$$\left[\chi_{ABA} \left(\frac{J_{AA}}{J_{BB}} \right) \right] \frac{J_{AB}}{J_{BB}} = a_1 \sqrt[4]{\frac{J_{AA}}{J_{BB}}} + b_1 \quad (15)$$

$$\left[\kappa_{ABA} \left(\frac{J_{AB}}{J_{BB}} \right) \right] \frac{J_{AA}}{J_{BB}} = c_1 \sqrt[4]{\left| \frac{J_{AB}}{J_{BB}} \right|} + d_1 \quad (16)$$

Here, the coefficients, a_1 and b_1 , are functions of $\frac{J_{AB}}{J_{BB}}$, and, c_1 and d_1 , are functions of $\frac{J_{AA}}{J_{BB}}$. Similarly, for the *AAB* configuration, we write two similar functional vari-

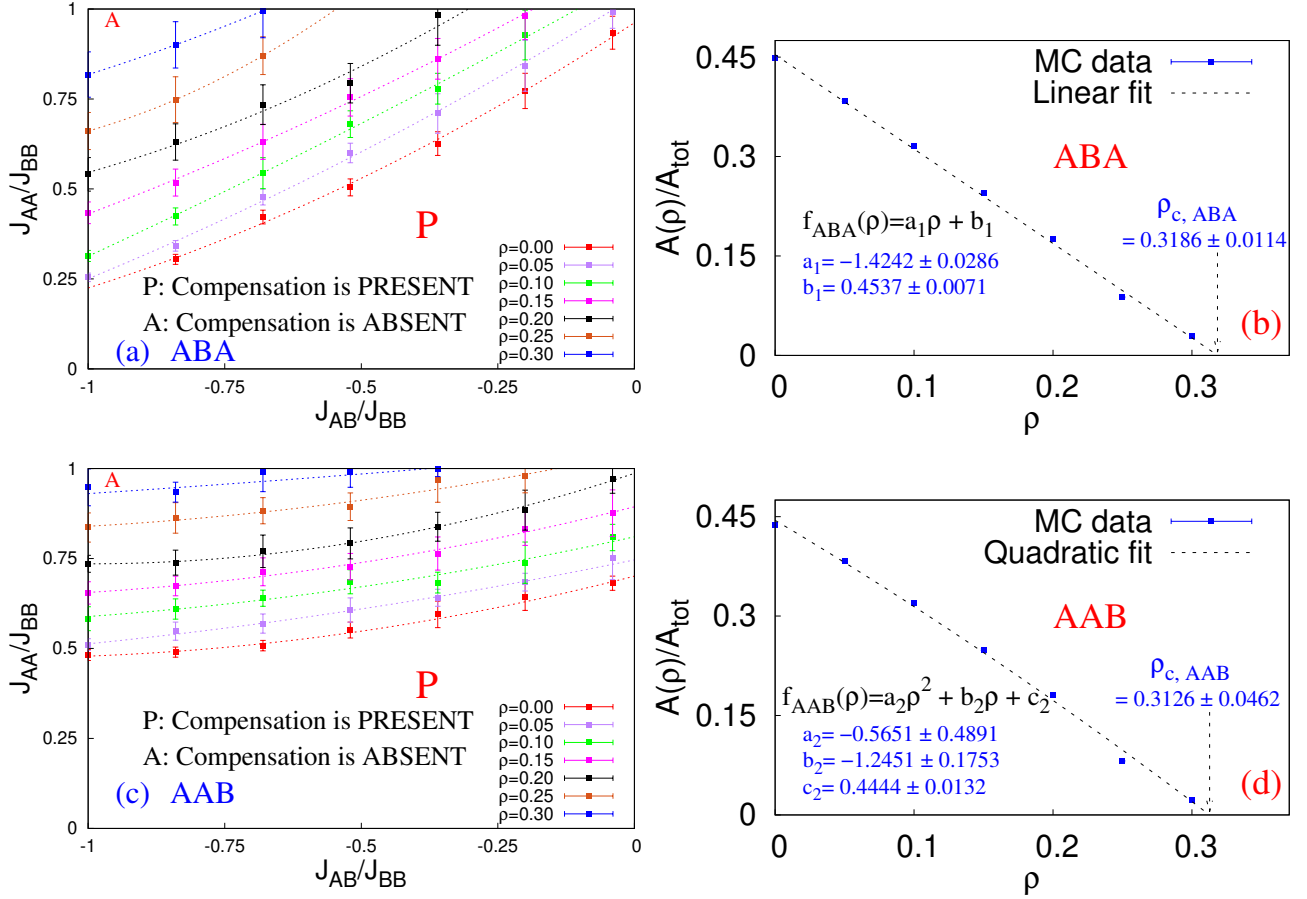


Figure 6: (Colour Online) Phase diagrams in the $(J_{AB}/J_{BB} \times J_{AA}/J_{BB})$ plane for: (a) ABA and (c) AAB configurations with concentration of nonmagnetic atoms acting as a parameter. The fractional area of the non-compensating region, $A(\rho)/A_{tot}$, as a function of concentration of non-magnetic impurities, ρ are plotted, for ABA configuration in (b) and for AAB configuration in (d).

ations.

$$\left[\chi_{AAB} \left(\frac{J_{AA}}{J_{BB}} \right) \right] \frac{J_{AB}}{J_{BB}} = a_2 \sqrt[4]{\frac{J_{AA}}{J_{BB}}} + b_2 \quad (17)$$

$$\left[\kappa_{AAB} \left(\frac{J_{AB}}{J_{BB}} \right) \right] \frac{J_{AA}}{J_{BB}} = c_2 \sqrt{\left| \frac{J_{AB}}{J_{BB}} \right|} + d_2 \quad (18)$$

As before, the coefficients, a_2 and b_2 , are functions of $\frac{J_{AB}}{J_{BB}}$, and, c_2 and d_2 , are functions of $\frac{J_{AA}}{J_{BB}}$. So, how would one find out the value of ρ_T , when $\frac{J_{AA}}{J_{BB}}$ and $\frac{J_{AB}}{J_{BB}}$ are given? One way is simply finding out the geometric mean of the functions, χ , and κ , e.g.

$$\rho_T \left(\frac{J_{AA}}{J_{BB}}, \frac{J_{AB}}{J_{BB}} \right) = \sqrt{\left[\chi \left(\frac{J_{AA}}{J_{BB}} \right) \right] \frac{J_{AB}}{J_{BB}} \left[\kappa \left(\frac{J_{AB}}{J_{BB}} \right) \right] \frac{J_{AA}}{J_{BB}}} \quad (19)$$

5 Summary

In this study, how site-dilution affects the formation of compensation points in a ferrimagnetic spin-1/2 Ising trilayered system on square monolayers, is investigated. The

ABA and AAB configurations have non-equivalent planes, meaning only the A-layers experience random site dilution, while the B-layer, which has the strongest in-plane coupling, remains pristine. Using Metropolis Monte Carlo simulations, we compared the diluted system to its pristine counterpart in their phase diagrams $(J_{AA}/J_{BB} \times J_{AB}/J_{BB})$ plane. The findings show that when a fixed amount of spin-0 impurities is introduced, the compensation point moves closer to the critical point and eventually merges with it as we increase the coupling ratios, just as it happens with the pristine configurations. On the other hand, if we keep the coupling ratios constant and increase the density of diluted sites, both the compensation and critical temperatures drop. This behavior is further supported by changes in magnetization, susceptibility and specific heat (Figure).

Interestingly, we found that the compensation temperature follows a quadratic trend with the concentration of non-magnetic atoms. Across all impurity levels, the system consistently undergoes continuous (second-order) phase transitions at the critical points. However, the most exciting observation is that adding impurities can actually create compensation points under certain combinations of coupling strengths. The minimum impurity concentration, ρ_T , needed to generate a compensation point depends on the coupling ratios in a parabolic way for both ABA and AAB configurations.

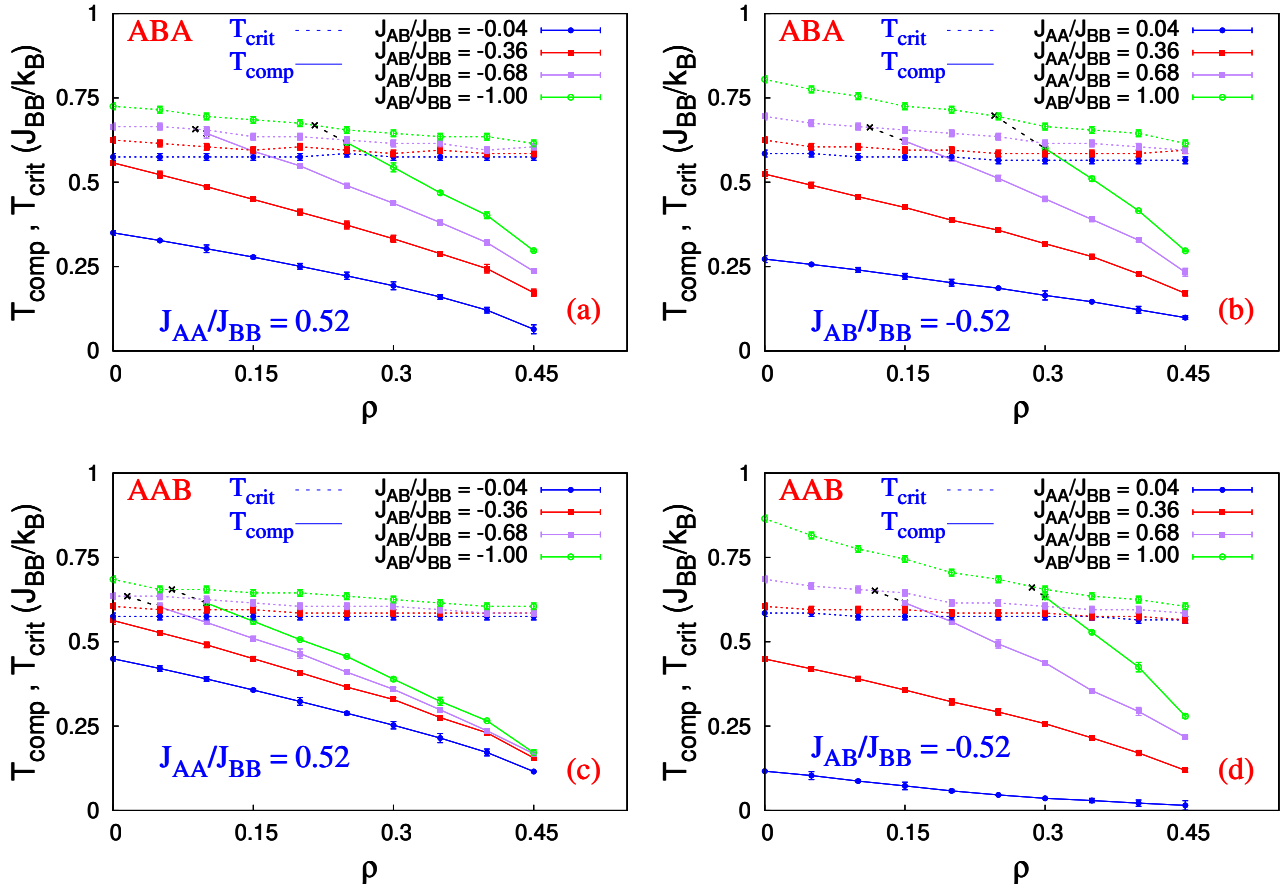


Figure 7: (Colour Online) Variation of Critical and Compensation temperatures with an increase in the concentration of nonmagnetic impurities for a few representative cases: for an ABA configuration in (a) and (b) and for an AAB configuration in (c) and (d). Where the errorbars are not visible, they are smaller than the point markers.

(a) ABA :					
$\left[\frac{J_{AA}}{J_{BB}}(\rho)\right]_{fit} = p_1(\rho) \left(\frac{J_{AB}}{J_{BB}}\right)^2 + q_1(\rho) \left(\frac{J_{AB}}{J_{BB}}\right) + r_1(\rho)$					
ρ	$p_1(\rho)$	$q_1(\rho)$	$r_1(\rho)$	χ^2/n_{dof}	p -value
0.00	0.255	0.992	0.962	0.416	0.742
0.05	0.158	0.943	1.035	0.338	0.852
0.10	0.072	0.846	1.087	0.087	0.967
0.15	0.145	0.871	1.156	0.044	0.988
0.20	0.318	1.067	1.295	0.308	0.735
0.25	0.686	1.806	1.781	-	-
0.30	0.234	0.948	1.531	-	-

(b) AAB :					
$\left[\frac{J_{AA}}{J_{BB}}(\rho)\right]_{fit} = p_2(\rho) \left(\frac{J_{AB}}{J_{BB}}\right)^2 + q_2(\rho) \left(\frac{J_{AB}}{J_{BB}}\right) + r_2(\rho)$					
ρ	$p_2(\rho)$	$q_2(\rho)$	$r_2(\rho)$	χ^2/n_{dof}	p -value
0.00	0.167	0.390	0.701	0.155	0.961
0.05	0.079	0.312	0.746	0.063	0.993
0.10	0.113	0.334	0.810	0.264	0.901
0.15	0.144	0.382	0.894	0.061	0.993
0.20	0.252	0.503	0.987	0.025	0.999
0.25	0.118	0.321	1.043	0.117	0.950
0.30	0.019	0.137	1.049	0.290	0.748

Table 1: Table of fitting parameters for phase curve of ABA and AAB trilayer configurations.

$\ln \left \frac{A(\rho)}{A} \right = ae^{b\rho}$					
type	a	b	$\ln \tilde{A}$	n_{dof}	$\frac{\chi^2}{n_{dof}}$
ABA	-0.1639 ± 0.0294	9.5092 ± 0.5583	-0.6829 ± 0.0574	4	0.0020
AAB	-0.1125 ± 0.0218	10.9771 ± 0.6172	-0.7587 ± 0.0530	4	0.0025

Table 2: Table of scaling parameters of Equation [14] for ABA and AAB trilayer configurations.

The mathematical models we developed help describe the system in detail, offering valuable insights into how dilution affects trilayered magnetic materials. These findings could contribute to future research on site-diluted magnetic systems with non-equivalent planes and different sublattice structures.

Acknowledgements

The author gratefully acknowledges financial assistance from the University Grants Commission, India in the form of a Research fellowship and extends his thanks to Dr. Tamaghna Maitra, Ms. Esha Lyngdoh and Dr. W L Reenbohn for providing the computational facilities and to Dr. Soumyajit Sarkar and Dr. Rupak Kumar Bhattacharya for their insightful comments.

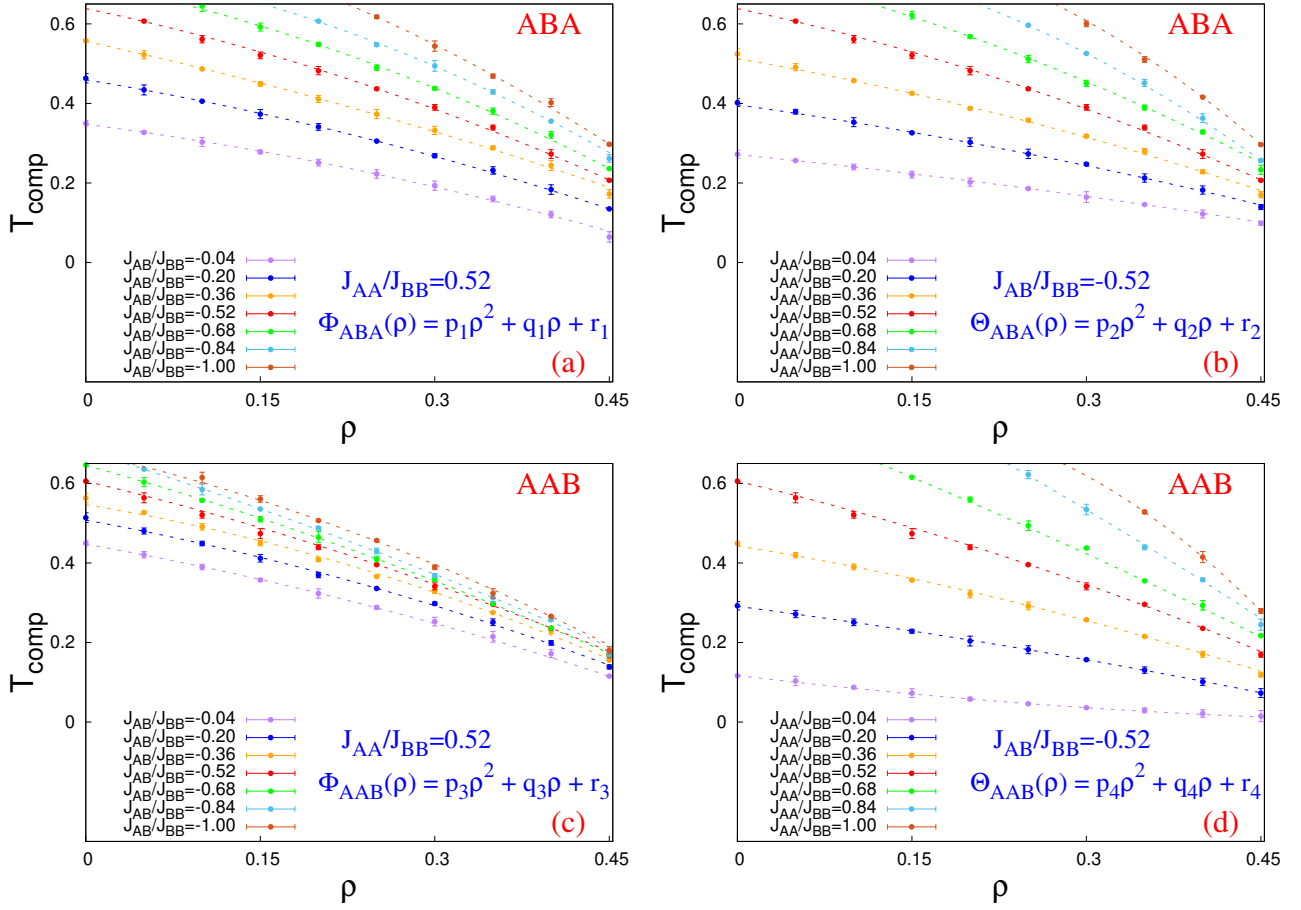


Figure 8: (Colour Online) The behaviour of the fitting quadratic polynomial for the variation of Compensation temperatures with an increase in the concentration of nonmagnetic impurities for a few representative cases: for an ABA configuration in (a) and (b) and for an AAB configuration in (c) and (d). Where the errorbars are not visible, they are smaller than the point markers.

References

1. Néel M. L., Ann. de Phys. **12**, 137 (1948).
2. Cullity B. D. and Graham C. D., Introduction to Magnetic Materials, 2nd edn. (Wiley, New York, 2008) .
3. Diaz I. J. L. and Branco N. S., Phys. B: Condens. Matter **529**, 73 (2018) .
4. Diaz I. J. L. and Branco N. S., Phys. A: Stat. Mech. Appl. **540**, 123014 (2020).
5. Chandra S. and Acharyya M., AIP Conf. Proc. **2220**, 130037 (2020) .
6. Chandra S., Eur. Phys. J. B **94**, 13 (2021) .
7. Chandra S., J. Phys. Chem. Solids **156**, 110165 (2021) .
8. Chandra S., Phys. Rev. E **104**, 064126 (2021) .
9. Chandra S., Eur. Phys. J. Plus **138**, 573 (2023) .
10. Chandra S., Phys. A **619**, 128737 (2023) .
11. Camley R. E. and Barnaś J., Phys. Rev. Lett. **63**, 664 (1989).
12. Connell G., Allen R. and Mansuripur M., J. Appl. Phys. **53**, 7759 (1982).
13. Phan M.-H. and Yu S.-C., Journal of Magnetism and Magnetic Materials **308**, 325 (2007).
14. Grünberg P., Schreiber R., Pang Y., Brodsky M. B. and Sowers H., Phys. Rev. Lett. **57**, 2442 (1986).
15. Stier M. and Nolting W., Phys. Rev. B **84**, 094417 (2011).
16. Smits C., Filip A., Swagten H., Koopmans B., De Jonge W., et al., Phys. Rev. B **69**, 224410 (2004).
17. Leiner J., Lee H., Yoo T., Lee S., Kirby B., et al., Phys. Rev. B **82**, 195205 (2010).
18. Chern G., Horng L., Shieh W. K., and Wu T. C., Phys. Rev. B **63**, 094421 (2001).
19. Sankowski P. and Kacman P., Phys. Rev. B **71**, 201303 (2005).
20. Chung J.-H., Song Y.-S., Yoo T., Chung S. J., Lee S., et al., Journal of Applied Physics **110**, 013912 (2011).
21. Samburskaya T., Sipatov A. Y., Volobuev V., Dziawa P., Knoff W., et al., Acta Phys. Pol. A **124**, 133 (2013).

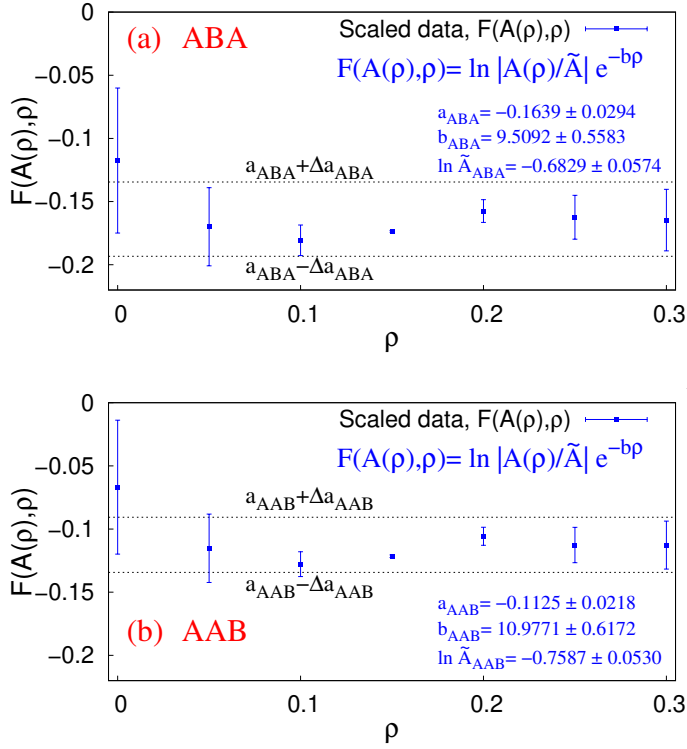


Figure 9: (Colour Online) Verification of *scaling behaviour* of: (A) ABA-type and (B) AAB-type site-diluted square trilayered ($N_{sites} = 3 \times 100 \times 100$) Ising superlattices.

22. Herman M. A. and Sitter H., Molecular beam epitaxy: fundamentals and current status, Vol. 7 (Springer Science & Business Media, 2012).
23. Stringfellow G. B., Organometallic vapor-phase epitaxy: theory and practice (Academic Press, 1999).
24. Singh R. K. and Narayan J., Phys. Rev. B **41**, 8843 (1990).
25. Leskelä M. and Ritala M., Angewandte Chemie International Edition **42**, 5548 (2003).
26. George S. M., Chem. Rev **110**, 111 (2010).
27. Tsubokawa I., J. Phys. Soc. Jpn. **15**, 1664 (1960).
28. Dillon J. F. and Olsen C. E., J. Appl. Phys. **36**, 1259 (1965).
29. Huang B., Clark G., Navarro-Moratalla E., Klein D. R., Cheng R., et. al., Nature **546**, 270 (2017).
30. Wang H., Eyert V. and Schwingenschlög U., J. Phys. Condens. Matter **23**, 116003 (2011).
31. Sivadas N., Okamoto S., Xu X., Fennie C. J. and Xiao D., Nano Lett. **18**, 7658 (2018).
32. Lado J. L. and J. Fernández-Rossier, 2D Mater. **4**, 035002 (2017).
33. Jiang P., Li L., Liao Z., Zhao Y. X. and Zhong Z., Nano Lett. **18**, 3844 (2018).
34. Zheng F., Zhao J., Liu Z., Li M., Zhou M., et. al., Nanoscale **10**, 14298 (2018).
35. Jang S. W., Jeong M. Y., Yoon H., Ryee S. and Han M. J., Phys. Rev. Mater. **3**, 031001 (2019).
36. Thiel L., Wang Z., Tschudin M. A., Rohner D., Gutiérrez-Lezama I., et. al., Science **364**, 973 (2019).
37. Ubrig N., Wang Z., Teyssier J., Taniguchi T., Watanabe K., et. al., 2D Mater. **7**, 015007 (2019).
38. Sarkar S., and Kratzer P., Phys. Rev. Mater. **4**, 104006 (2020).
39. Sarkar S., and Kratzer P., Phys. Rev. B **103**, 224421 (2021).
40. Amaral J. S., Silva N. J. O. and Amaral V. S., Appl. Phys. Lett. **91**, 172503 (2007).
41. Franco V., Conde A., Romero-Enrique J. M. and Blázquez J. S., J. Phys.: Condens. Matter **20**, 285207 (2008).
42. Dong Q. Y., Zhang H. W., Sun J. R., Shen B. G. and Franco V., J. Appl. Phys. **103**, 116101 (2008).
43. de Oliveira N. and von Ranke P., Phys. Rep. **489**, 89 (2010).
44. Amaral J. S. and Amaral V. S. in : *Thermodynamics: Systems in Equilibrium and Non-Equilibrium*, ed. Moreno-Piraján J. C., chapter 8, pp. 173-198 (2011).
45. Franco V., Blazquez J. S., Ingale B. and Conde A., Annu. Rev. Mater. Res. **42**, 305 (2012).
46. Pełka R., et al., Acta Phys. Pol. A **124**, 977 (2013).
47. Čanová L., Strečka J. and Jaščur M. 2006 J. Phys.: Condens. Matter **18**, 4967 (2006).
48. Pereira M. S. S., de Moura F. A. B. F. and Lyra M. L., Phys. Rev. B **79**, 054427 (2009).
49. Ohanyan V. and Honecker A., Phys. Rev. B **86**, 054412 (2012).
50. Gálisová L., Condens. Matter Phys. **17**, 13001 (2014).
51. Strečka J., Physica A **360**, 379 (2006).
52. Ribeiro G. A. P., J. Stat. Mech. **2010**, P12016 (2010).
53. Trippe C., Honecker A., Klümper A. and Ohanyan V., Phys. Rev. B **81**, 054402 (2010).
54. Zhitomirsky M. E. and Honecker A. 2004 J. Stat. Mech. **2004**, P07012 (2004).
55. Topilko M., Krokhmalkii T., Derzhko O. and Ohanyan V., Eur. Phys. J. B **85**, 1 (2012).
56. Oliveira S., Morais R. H. M., Santos J. P. and Sá Barreto F. C., Condens Matter Phys., **25(1)**, 13702 (2022).
57. Guru E. and Saha S., Phase Transit., (2022); DOI: 10.1080/01411594.2022.2095274 .

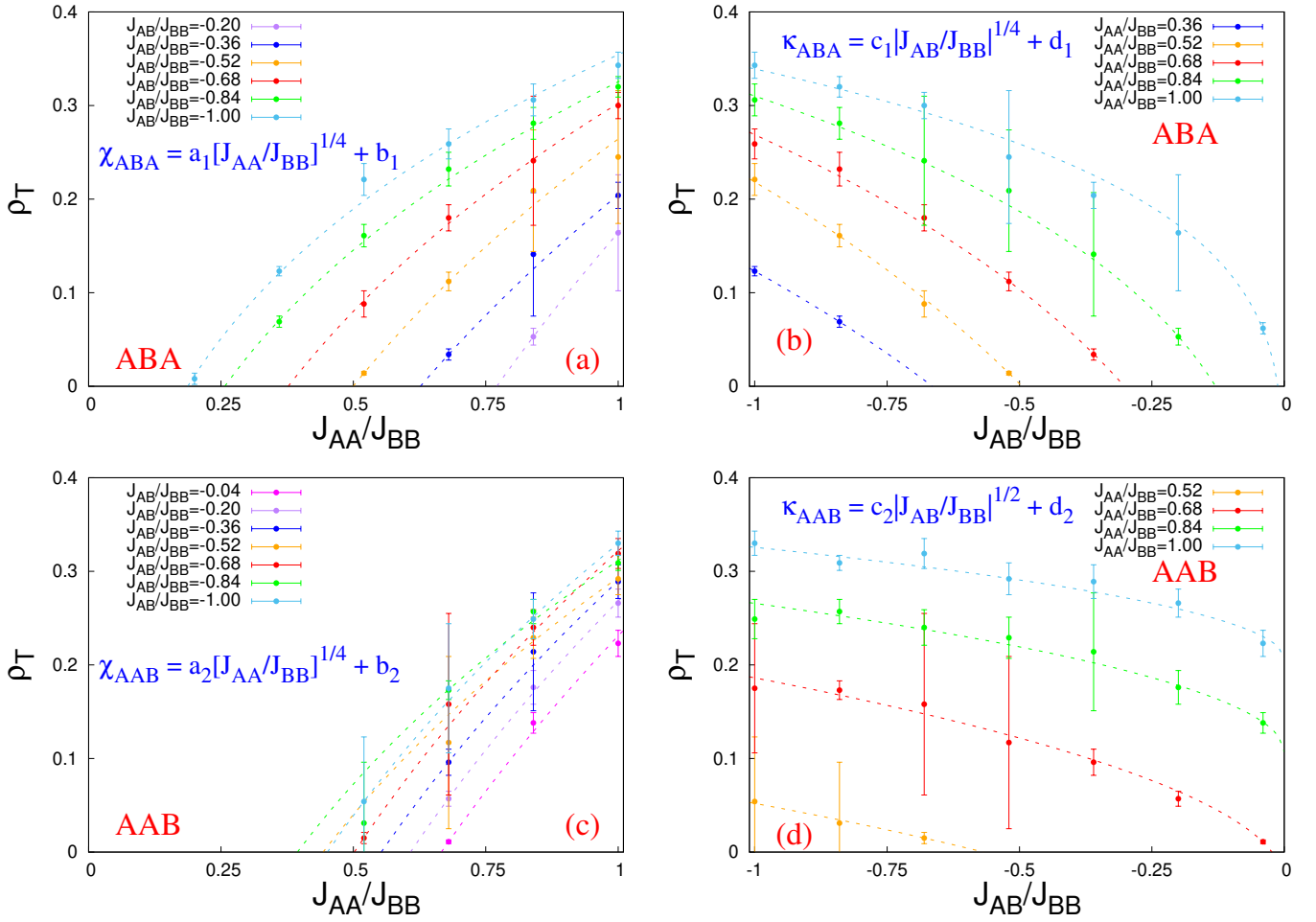


Figure 10: (Colour Online) Plots of threshold concentration, ρ_T of spin-0 impurities versus Hamiltonian parameters: (a) ρ_T versus J_{AA}/J_{BB} and (b) ρ_T versus J_{AB}/J_{BB} , for an ABA configuration and (c) ρ_T versus J_{AA}/J_{BB} and (d) ρ_T versus J_{AB}/J_{BB} , for an ABA configuration.

58. Guru E., Saha S. and Nag S., arXiv preprint, arXiv:2412.21198
59. Sandeman K. G., Scr. Mater. **67**, 566 (2012).
60. Manosa L., Planes A. and Acet M., J. Mater. Chem. A **1**, 4925 (2013).
61. Aydiner E., Yüksel Y., Kis-Cam E., and Polat H., J. Magn. Magn. Mater. **321**, 3193 (2009).
62. Diaz I. J. L. and Branco N. S., Phys. A **468**, 158 (2017).
63. Diaz I. J. L. and Branco N. S., Physica A **490**, 904 (2018).
64. Ising E., Z. Phys. **31**, 253 (1925).
65. Landau D. P. and Binder K., A Guide to Monte Carlo Simulations in Statistical Physics (Cambridge University Press, New York, 2000).
66. Binder K. and Heermann D. W., Monte Carlo Simulation in Statistical Physics (Springer, New York, 1997).
67. Newman M. E. J. and Barkema G. T., Monte Carlo Methods in Statistical Physics (Oxford University Press, New York, 2001).
68. Krauth W., Statistical Mechanics: Algorithms and Computations (Oxford University Press, UK, 2006)
69. Chikazumi S., Physics of Ferromagnetism (Oxford University Press, Oxford, 1997).
70. Miyazaki T. and Jin H., The Physics of Ferromagnetism (Springer Series in Materials Science 158, 2012)
71. Scarborough J.B., Numerical Mathematical Analysis, (Oxford & Ibh, London, 2005).
72. Press W. H., Teukolsky S. A., Vetterling W. T. and Flannery B. P., Numerical Recipes: The Art of Scientific Computing (Cambridge University Press, Cambridge, UK, 2007)
73. Ferrenberg A. M. and Landau D. P., Phys. Rev. B **44** (10), 5081 (1991).